Kobayashi *et al. Earth, Planets and Space* (2016) 68:66
DOI 10.1186/s40623-016-0441-1

Earth, Planets and Space

LETTER

Open Access

Joint inversion of teleseismic, geodetic, and near-field waveform datasets for rupture process of the 2015 Gorkha, Nepal, earthquake

Hiroaki Kobayashi[1*], Kazuki Koketsu[1], Hiroe Miyake[1], Nobuo Takai[2], Michiko Shigefuji[3,4], Mukunda Bhattarai[5] and Soma Nath Sapkota[5]

Abstract

The 2015 Gorkha earthquake and its aftershocks caused severe damage mostly in Nepal, while countries around the Himalayan region were warned for decades about large Himalayan earthquakes and the seismic vulnerability of these countries. However, the magnitude of the Gorkha earthquake was smaller than those of historical earthquakes in Nepal, and the most severe damage occurred in the north and northeast of Kathmandu. We explore reasons for these unexpected features by performing a joint source inversion of teleseismic, geodetic, and near-field waveform datasets to investigate the rupture process. Results indicate that the source fault was limited to the northern part of central Nepal and did not reach the Main Frontal Thrust. The zone of large slip was located in the north of Kathmandu, and the fault rupture propagated eastward with an almost constant velocity. Changes in the Coulomb failure function (ΔCFF) due to the Gorkha earthquake were computed, indicating that southern and western regions neighboring the source fault are potential source regions for future earthquakes related to the Gorkha earthquake. These two regions may correspond to the historical earthquakes of 1866 and 1344. Possible future earthquakes in the regions are predicted, and the warning for Himalayan seismic hazards remains high even after the Gorkha earthquake.

Keywords: Rupture process, Gorkha earthquake, Coulomb failure function

Background

Around Nepal, the Indian and Eurasian plates collide, and the Indian lithosphere underthrusts beneath the Eurasian plate at the Main Frontal Thrust (MFT, Fig. 1) with a convergence rate of approximately 18 mm/year (Ader et al. 2012). This has historically caused large earthquakes, and seismic hazards in the region remain high (Bilham et al. 2001; Bilham and Gaur 2013). On April 25, 2015 (UTC), the Gorkha earthquake occurred close to Katmandu. The hypocenter of the earthquake determined by the United States Geological Survey (USGS, http://www.usgs.gov/, accessed on April 27, 2015) was 28.1473°N, 84.7079°E, and 15 km in depth, indicating that the earthquake occurred on the Main Himalayan Thrust (MHT). The earthquake and its aftershocks resulted in over 8000 fatalities. The moment magnitude (M_w) of this earthquake (7.8; USGS) was smaller than those of historical earthquakes in Nepal, such as the M_w 8.2 1505 Lo Mustang earthquake and the M_w 8.1 1934 Bihar–Nepal earthquake (Ambraseys and Douglas 2004). Moreover, although its hypocenter was located in the northwest of Kathmandu, the most severe damage occurred in the north and northeast of Kathmandu (Government of Nepal 2015). Therefore, an investigation of the rupture process of the Gorkha earthquake is crucial to explore potential reasons underlying these peculiar features. Previous source studies of the Gorkha earthquake were performed using teleseismic waveforms (Fan and Shearer 2015; Yagi and Okuwaki 2015); InSAR (Kobayashi et al. 2015; Lindsey et al. 2015); teleseismic waveforms and InSAR (Avouac et al. 2015; Hayes et al. 2015); static GPS and InSAR (Feng et al. 2015; Wang and Fialko 2015); static GPS, high-rate GPS, and InSAR (Galetzka et al. 2015); teleseismic

*Correspondence: khiro@eri.u-tokyo.ac.jp
[1] Earthquake Research Institute, University of Tokyo, 1-1-1 Yayoi, Bunkyo-ku, Tokyo, Japan
Full list of author information is available at the end of the article

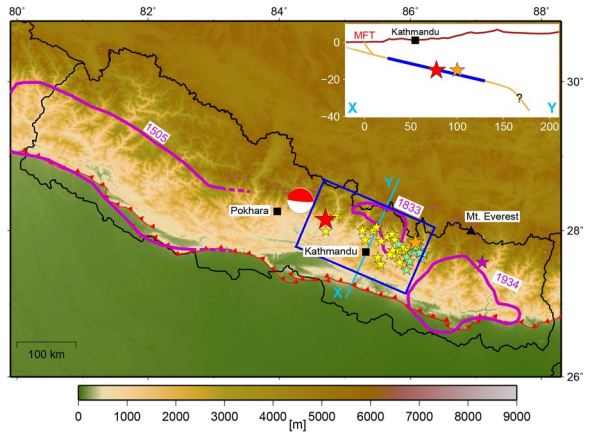

Fig. 1 Index map. Epicenters of the main shock and the largest aftershock are indicated by *red* and *orange stars*. The focal mechanism of the main shock is shown in the map. *Small yellow* and *green stars* denote aftershocks within 6 h after the main shock and largest aftershock, respectively. We locate the source fault of the earthquake as shown by the *blue rectangle*. Areas outlined in *magenta* indicate the assumed source region of the 1505 earthquake (Bilham and Ambraseys 2005), with the eastern extent determined by Bollinger et al. (2014) and the zones of VIII or greater intensities for the 1833 and 1934 earthquakes (Bollinger et al. 2014; Sapkota et al. 2013). The epicenter of the 1934 earthquake is indicated by the *magenta star* (Sapkota et al. 2013). *Red curves* with *triangles* represent the Main Frontal Thrust (MFT). The *upper-right inset* shows the cross-sectional profile along the *sky blue line* including the MFT and the schematic Main Himalayan Thrust (MHT) (*light brown line*; Bollinger et al. 2014). *Background color* indicates altitude

waveforms, strong motion, static GPS, high-rate GPS, and InSAR (Grandin et al. 2015); and teleseismic waveforms, static GPS, and high-rate GPS (Kubo et al. 2016). Near-field waveforms are most effective to investigate the spatiotemporal earthquake rupture process. Takai et al. (2016) succeeded in observing the main shock ground motions at four strong motion stations in the Kathmandu Valley (Fig. 2a). One of these stations, KTP, is located at a rock site, as implied by the observed waveforms with weak latter phases (Fig. 2b). Previous studies only used initial parts or a quite low-frequency range of near-field waveforms in the Kathmandu Valley from high-rate GPS and strong motion stations. These stations are located on soft sediment and latter phase are strongly affected by sedimentary layers whose velocity structure is not well known. Thus, we used KTP instead of stations on soft sediment and performed a joint inversion of teleseismic, geodetic, and near-field waveform datasets to investigate the rupture process of the Gorkha earthquake. We also calculated the Coulomb failure function (ΔCFF) using the obtained results to evaluate the effect of the Gorkha earthquake on surrounding regions.

Joint source inversion

Three types of datasets are available for this investigation: (1) teleseismic dataset obtained from the Global Seismographic Network (Fig. 2c) through the Data Management Center of the Incorporated Research Institutions for Seismology, (2) ground deformation dataset obtained at GPS stations (Fig. 2a) through the UNAVCO Data Center and from the InSAR image processed by Lindsey et al. (2015), and (3) dataset of near-field waveforms of strong motion (Takai et al. 2016) and high-rate GPS (Galetzka et al. 2015) stations (Fig. 2a). We used 37 vertical components of a teleseismic P wave, 12 horizontal components of six GPS stations and four vertical components of four GPS stations, line-of-sight deformations of 21 points from the InSAR image, and 18 components of six strong motion and high-rate GPS stations. We downsampled the InSAR image while keeping rough characteristics with intervals of 0.2°, a larger interval than the discretization of our fault model. We then selected points whose absolute line-of-sight deformations were greater than 10 cm. We did not use near-field waveforms of TVU, PTN, THM, and NAST because they are located on soft sediment and their waveforms, especially their horizontal components, are largely affected by sedimentary layers. Moreover, a detailed velocity structure of the Kathmandu Valley was not established.

First, the source fault was defined based on the hypocenter distribution of the main shock and aftershocks from the USGS data, as shown by the blue rectangle in Fig. 1. Strike and dip angles were set to 293° and 7°, the same as the Global CMT solution. The fact that the source fault region is limited to the northern part of central Nepal was inferred as the main reason for the smaller M_w of the Gorkha earthquake in comparison with historical earthquakes, such as the M_w 8.2 1505 Lo Mustang earthquake and the M_w 8.1 1934 Bihar–Nepal earthquake (Ambraseys and Douglas 2004). Subsequently, a joint inversion of the abovementioned three datasets was performed to determine the rupture process of the Gorkha earthquake.

For this purpose, we used the multi-time-window linear inversion method with nonnegative least squares and smoothness constraints (Yoshida et al. 1996; Hikima and Koketsu 2005). We divided a fault into 18 × 11 subfaults with a size of 10 km in length and 10 km in width. Six 3-s ramp functions for the fault slip were set every 3 s for each subfault. The optimal number of time windows and their duration were determined by a trial-and-error approach. Rake angles were varied between 90° ± 45°. We determined the rupture front velocity, which controls the timing of the first time window to be 3.3 km/s, because this value minimized the teleseismic and near-field

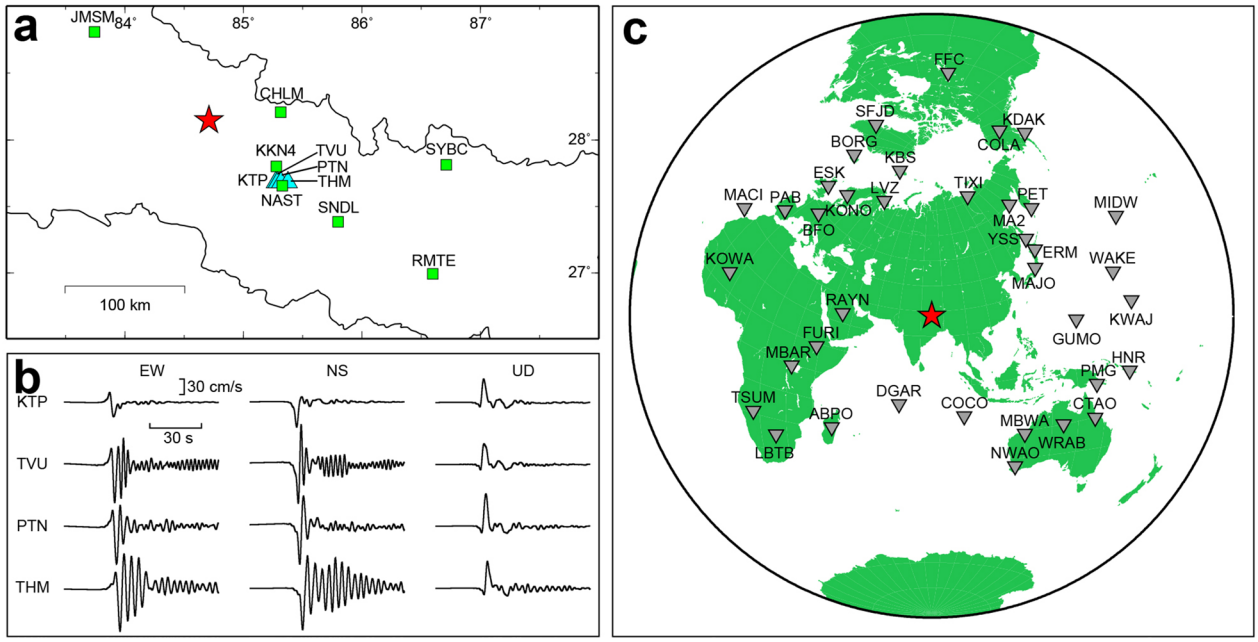

Fig. 2 **a** Strong motion and geodetic station map. *Red star* denotes the main shock epicenter. *Sky blue triangles* indicate strong motion stations. *Green squares* indicate high-rate and static GPS stations. **b** Filtered (0.005–0.4 Hz, the frequency range of our inversion analysis) velocity waveforms at four strong motion stations. All the waveforms are plotted using the same scale. **c** Teleseismic stations map. *Red star* denotes the main shock epicenter. *Gray reverse triangles* indicate teleseismic stations

waveform variance. The weight of spatiotemporal smoothness constraints was determined by minimizing the Akaike's Bayesian information criterion (Akaike 1980). The weights of all data points were set equal after flattening square values of each data point. Teleseismic, geodetic, and near-field waveform Green's functions were computed by the methods of Kikuchi and Kanamori (2003), Zhu and Rivera (2002), and Kohketsu (1985), respectively. One-dimensional velocity structure model of CRUST 2.0 (Bassin et al. 2000) was used for these calculations. In this model, Vs around the source depth was 3.5 km/s. As such, the determined rupture front velocity was approximately 90 % of the local shear wave speed, indicating fast rupture propagation if rupture is primarily triggered in the first time window. In near-field waveform data processing, we integrated acceleration or differentiated displacement waveforms to velocity. In teleseismic data processing, we removed instrument response and integrated to displacement. All waveforms were band-pass-filtered between 0.005 and 0.4 Hz and resampled every 0.5 s. We used previously published geodetic data as it is.

The resulting total slip distribution with a maximum value of 7.0 m is shown in Fig. 3a. Two other slip peaks with 6.0 and 5.0 m are also obtained in the northeast of Kathmandu. These slip peaks are probably one of the main reasons for the severe damage in the north and northeast of Kathmandu. Moreover, these multiple slip peaks are consistent with the observed teleseismic and near-field waveforms, which have multiple amplitude peaks (Fig. 4a), such as the UD component of KTP that has a small secondary amplitude peak (Fig. 4b). There is a slip of 4.8 m at the southeast edge of the source fault. We confirmed that this slip is inferred from the InSAR data, specifically by two southeast data points (Fig. 4e). The centroid of the M_w 6.7 aftershock that occurred 1 day after the main shock, determined by the Global CMT solution, is located where the slip of 4.8 m was obtained, and the InSAR data include the effect of the aftershock. Thus, this slip might be an artifact of the main shock rupture process. Similarly, the M 6.1 earthquake that occurred 4 min after the main shock at about 20 km east of Kathmandu affects the InSAR data, but we cannot evaluate the magnitude of the effect. The calculated seismic moment is 7.4×10^{20} Nm, which yields an M_w of 7.8. Snapshots of the slip distribution are taken every 10 s after rupture initiation at the hypocenter (Fig. 3b), showing that the fault rupture propagates eastward at an almost constant velocity and then in two directions at 30–40 s. The moment rate function (Fig. 3c) shows that the total rupture duration is about 60 s with a peak at approximately 35 s. Considering the snapshots, the peak corresponds to the two slips in the northeast of Kathmandu. Slip rate functions of each subfault show

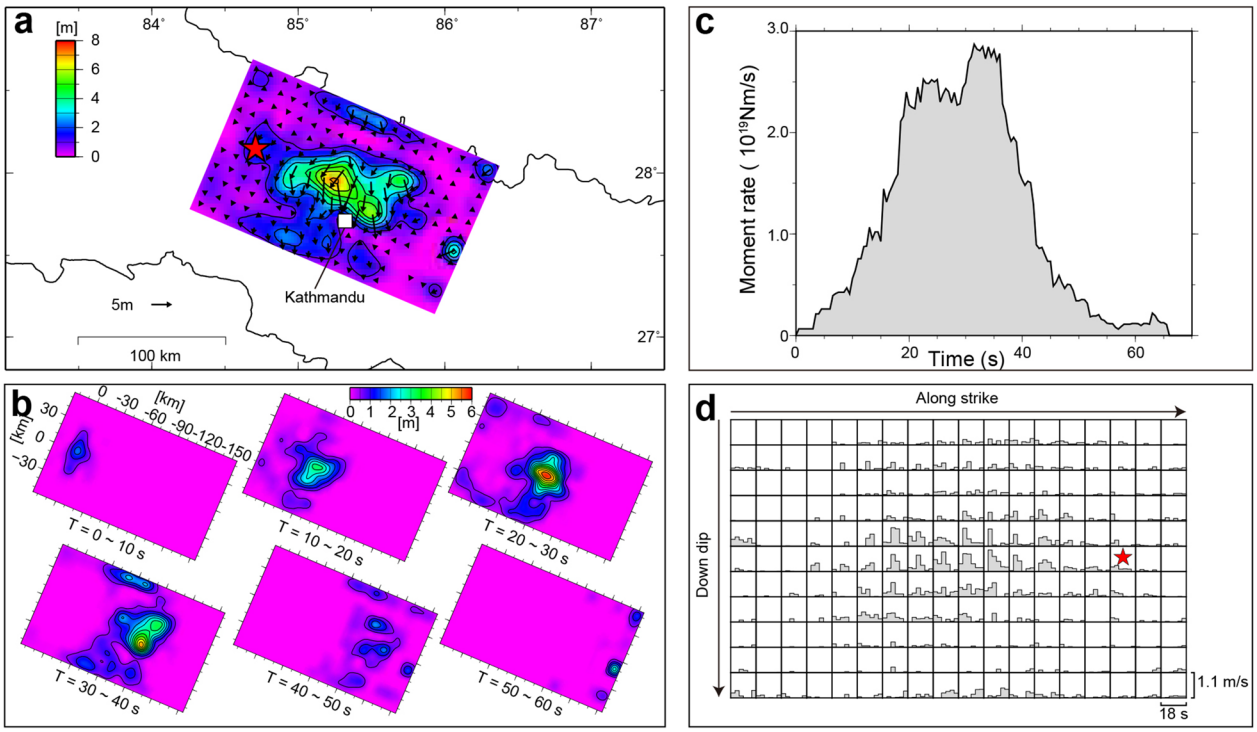

Fig. 3 **a** Distribution of resulting total slips with 1-m contour interval from the joint source inversion. *Red star* and *white rectangle* indicate the main shock epicenter and Kathmandu, respectively. **b** Snapshots of slip distribution every 10 s with 0.5-m contour interval. **c** Final moment rate function. **d** Resulting slip rate function of each subfault. *Red star* denotes the main shock epicenter

that slips mostly start in the first or second time window around the largest slip area (Fig. 3d), indicating fast rupture propagation of approximately 3.0 km/s. Observed and synthetic waveforms and crustal deformation are shown in Fig. 4a–e. Most datasets fit well, but some near-field horizontal waveform fittings suggest that we need to improve the assumed velocity structure model.

To evaluate the resolution of each dataset and our joint source inversion analysis, we conducted checkerboard resolution tests using the same previously determined parameters. First, we set a target model, as shown in Fig. 5a, and made synthetic datasets. Then, we performed three inversions with (1) only teleseismic dataset; (2) teleseismic and geodetic datasets; and (3) teleseismic, geodetics, and near-field waveform datasets. The results of the first and second inversions show that the teleseismic dataset can reproduce the moment rate function and geodetic dataset to improve the spatial resolution (Fig. 5b, c). The results of the third inversion show that our joint inversion analysis has a sufficient spatiotemporal resolution (Fig. 5d).

Source process analysis by Grandin et al. (2015) is most similar in terms of datasets. The difference between their and our resulting slip distribution is that over 4 m slip area expanded to about 50 km east of Kathmandu is only seen in Grandin et al. (2015). This slip can be observed in other studies that used InSAR data (Feng et al. 2015; Galetzka et al. 2015; Hayes et al. 2015; Kobayashi et al. 2015; Lindsey et al. 2015; Wang and Fialko 2015); however, Avouac et al. (2015) also used InSAR data, and their resulting slip distribution does not show the slip in question. This is probably because one of the two InSAR images used by Avouac et al. (2015) does not cover the eastern region of Kathmandu. As mentioned previously, the M 6.1 and M_w 6.7 aftershocks occurred in the east of Kathmandu. InSAR data are very dense to include local deformation by the aftershocks. Our discretization of InSAR data probably reduced the effects of the aftershocks.

Relation between the Gorkha earthquake and future earthquakes

To examine the relation between the Gorkha earthquake and potential future earthquakes in Nepal, changes in the ΔCFF (Reasenberg and Simpson 1992) were computed. The computation was performed for receiver faults with the focal mechanism of (strike, dip, rake) = (293°, 7°, 90°) along the plate boundary shown in the inset of Fig. 1. The results of the computation show that in Fig. 6, red zones of a large positive ΔCFF are distributed in small-slip

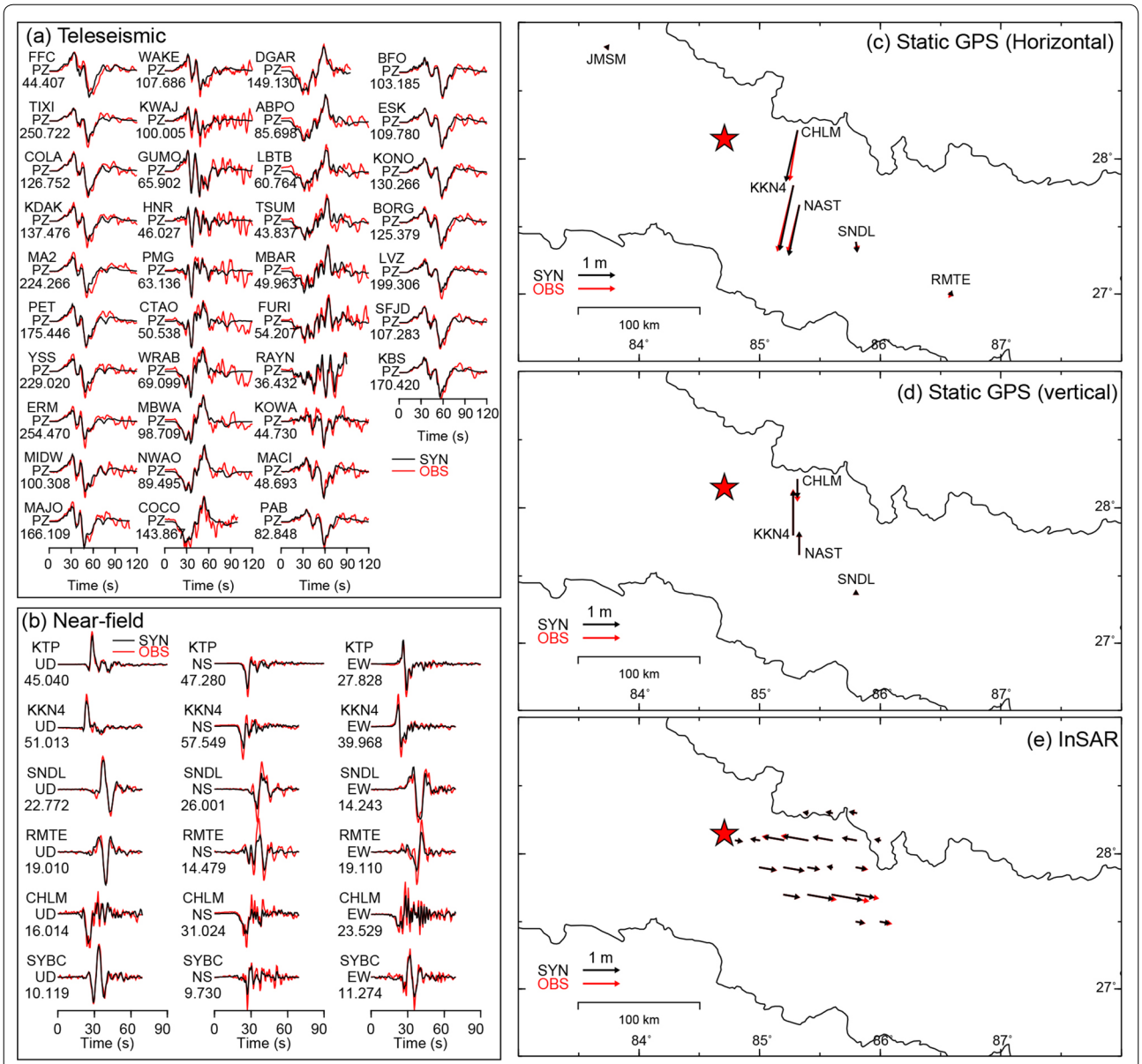

Fig. 4 Observed (*red*) and synthetic (*black*) waveforms at **a** teleseismic stations and **b** strong motion and high-rate GPS stations. Station code, component, and peak amplitude (micrometer for teleseismic and centimeter for near-field) are written on the *left* of each waveform. Observed (*red*) and synthetic (*black*) ground deformations from **c** horizontal component of static GPS, **d** vertical component of static GPS, and **e** InSAR. Line-of-sight deformations were derived from the processed InSAR images (Lindsey et al. 2015) and are used for the joint source inversion. *Red star* denotes the main shock epicenter

areas within the source fault (Fig. 3a) and in all regions surrounding this fault. The ΔCFF features of these surrounding regions are different from those reported by Feng et al. (2015) because they calculated the ΔCFF at a fixed depth. We note that the largest aftershock occurred in the red zone within the source fault of the main shock (Fig. 6).

Here, we focus on regions surrounding the source fault because we cannot discuss potential future earthquakes only through ΔCFF. No large earthquake is expected in the northern deeper part because this part is creeping (Mugnier et al. 2013), and the M_w 8.1 1934 Bihar–Nepal earthquake (Ambraseys and Douglas 2004) already occurred in the eastern region (Sapkota et al. 2013).

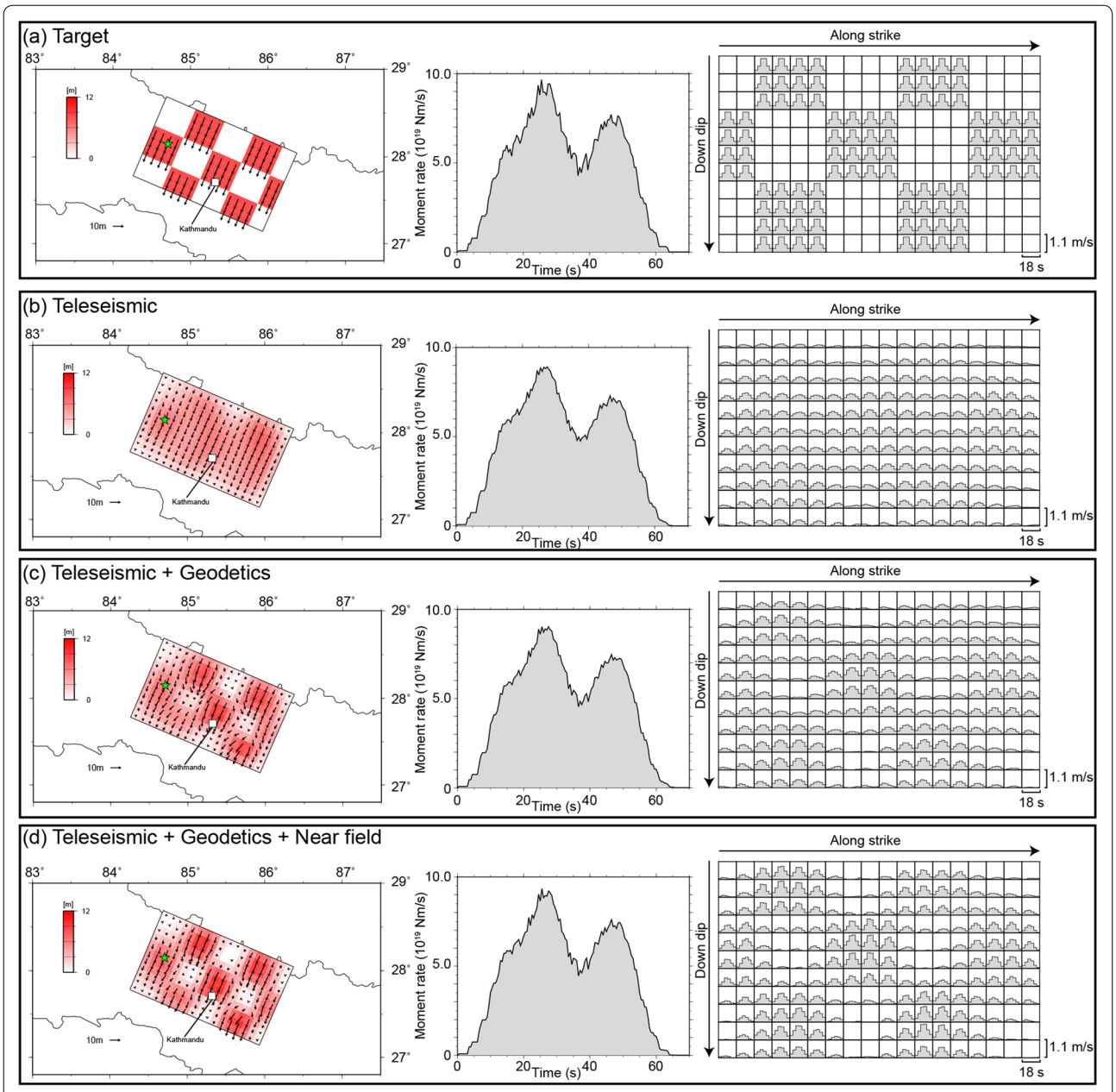

Fig. 5 **a** Slip distribution (*left*), moment rate function (*middle*), and slip rate function of each subfault (*right*) for the target model of checkerboard resolution test, and the inversion results of the checkerboard resolution tests of **b** teleseismic, **c** teleseismic and geodetics, and **d** teleseismic, geodetics, and near-field waveforms. *Green star* and *white rectangle* indicate the main shock epicenter and Kathmandu, respectively

Considering that the convergence rate and interseismic coupling between the Indian and Eurasian plates are spatially uniform in Nepal (Ader et al. 2012), remaining southern and western regions (dashed magenta ellipses in Fig. 6) might correspond to large earthquakes listed in the history of earthquakes damaging Kathmandu (Mugnier et al. 2013) and recent earthquakes felt in India (Szeliga et al. 2010). The 1866 earthquake (*M* 7.2 or 7.6) occurred in the southern region (Khattri 1987; Szeliga et al. 2010), and trenching at the MFT in the western region showed an event in the thirteenth or fourteenth century (Mugnier et al. 2013). These southern and western regions where historical earthquakes in 1866 and 1344 occurred were likely stimulated by the Gorkha earthquake, increasing the possibility of generating a large earthquake. Between the two regions, the calculated

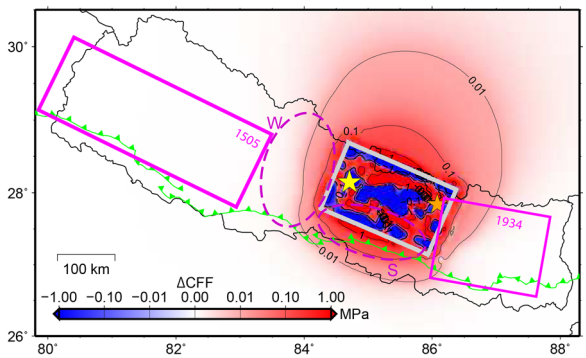

Fig. 6 Distribution of ΔCFF due to the Gorkha earthquake. Areas with positive and negative ΔCFF are *colored red* and *blue*, respectively. *Yellow* and *orange stars* denote the main shock epicenter and the largest aftershock epicenter, respectively. *Gray rectangle* represents source fault defined for the main shock, and *magenta rectangles* are those obtained for the 1934 and 1505 earthquakes from the zone of VIII or greater intensities, assumed source region, and the epicenter in Fig. 1. Their areas were calculated using scaling law between rupture areas and M_w (Murotani et al. 2008). *Green curves* with *triangles* denote the MFT. *Dashed magenta ellipses with letters* "S" and "W" in positive ΔCFF areas indicate potential source regions for future large earthquakes likely affected by the Gorkha earthquake

maximum ΔCFF of the southern region is one order of magnitude larger than that of the western region. Thus, the southern region was more likely stimulated.

In view of the abovementioned details, three scenarios were considered related to the Gorkha earthquake. First, if the entire western region was ruptured reaching up to the MFT, an *M*8-class earthquake, such as the 1934 Bihar–Nepal earthquake, would occur in accordance with its area (e.g., Murotani et al. 2008). Second, if the western region was ruptured with a partially similar situation to the Gorkha earthquake, an *M*7-class earthquake, such as the Gorkha earthquake, would occur. Third, if the southern region was ruptured, an *M*7-class earthquake, such as the 1866 earthquake, would occur. Galetzka et al. (2015) reported that the Gorkha earthquake was modest over a short period and large over a long period. The abovementioned three scenarios are plausible future earthquakes in this region, but it cannot be predicted if they will have the same features as the Gorkha earthquake.

Conclusions

Our inversion results show that the Gorkha earthquake mainly ruptured a relatively deeper part of the MHT with maximum slip in the north of Kathmandu. The total rupture duration was approximately 60 s, and the rupture propagates at a relatively high speed of approximately 3.0 km/s. The calculated ΔCFF from the Gorkha earthquake suggests three possible scenarios in the southern and western regions for the source fault of this earthquake. Thus, a warning of high Himalayan seismic hazards, which may include the three scenario earthquakes, should be continually issued to Nepal and countries around the Himalayas.

Authors' contributions

HK conducted the analysis. HK, KK, and HM drafted the manuscript. NT and MS acquired the strong motion data at the Kathmandu Valley and participated in the discussion. MB and SNS participated in the interpretation. All authors read and approved the final manuscript.

Author details

[1] Earthquake Research Institute, University of Tokyo, 1-1-1 Yayoi, Bunkyo-ku, Tokyo, Japan. [2] Faculty of Engineering, Hokkaido University, Kita 13, Nishi 8, Kita-ku, Sapporo, Japan. [3] Faculty of Science, Hokkaido University, Kita 10, Nishi 8, Kita-ku, Sapporo, Japan. [4] Present Address: Kyushu University, Fukuoka, Japan. [5] Department of Mines and Geology, Lainchour, Kathmandu, Nepal.

Acknowledgements

We would like to thank Yasuhiro Kumahara and Seiji Tsuno for providing us the data of MFT and the instrumental response of strong motion sensors, respectively. We also thank Martin Mai and two anonymous reviewers for their helpful comments. We used the Generic Mapping Tools (Wessel and Smith 1991) for drawing the figures. This study was supported by the SATREPS program of JST/JICA, the J-RAPID program of JST, and MEXT KAKENHI.

Competing interests

The authors declare that they have no competing interests.

Received: 31 October 2015 Accepted: 11 April 2016
Published online: 26 April 2016

References

Ader T, Avouac JP, Zeng JL, Caen HL, Bollinger L, Galetzka J, Genrich J, Thomas M, Chanard K, Sapkota SN, Rajaure S, Shrestha P, Ding L, Flouzat M (2012) Convergence rate across the Nepal Himalaya and interseismic coupling on the Main Himalayan Thrust: implications for seismic hazard. J Geophys Res 117:B04403. doi:10.1029/2011JB009071

Akaike H (1980) Likelihood and the Bayes procedure. Trabajos de Estadistica y de Investigacion Operativa 31:143–166. doi:10.1007/BF02888350

Ambraseys NN, Douglas J (2004) Magnitude calibration of north Indian earthquakes. Geophys J Int 159:165–206. doi:10.1111/j.1365-246X.2004.02323.x

Avouac JP, Meng L, Wei S, Wang T, Ampuero JP (2015) Lower edge of locked Main Himalayan Thrust unzipped by 2015 Gorkha earthquake. Nat Geosci 8:708–711. doi:10.1038/ngeo2518

Bassin C, Laske G, Masters G (2000) The current limits of resolution for surface wave tomography in North America. EOS Trans AGU 81:F897

Bilham R, Ambraseys N (2005) Apparent Himalayan slip deficit from the summation of seismic moments for Himalayan earthquakes, 1500–2000. Curr Sci 88:1658–1663

Bilham R, Gaur V (2013) Buildings as weapons of mass destruction. Science 341:618–619. doi:10.1126/science.1238476

Bilham R, Gaur VK, Molnar P (2001) Himalayan seismic hazard. Science 293:1442–1444. doi:10.1126/science.1062584

Bollinger L, Sapkota SN, Tapponnier P, Klinger Y, Rizza M, Van der Woerd J, Tiwari DR, Pandey R, Bitri A, Bes de Berc S (2014) Estimating the return times of great Himalayan earthquakes in eastern Nepal: evidence from the Patu and Bardibas strands of the Main Frontal Thrust. J Geophys Res 119:7123–7163. doi:10.1002/2014JB010970

Fan W, Shearer PM (2015) Detailed rupture imaging of the 25 April 2015 Nepal earthquake using teleseismic P waves. Geophys Res Lett. doi:10.1002/2015GL064587

Feng G, Li Z, Shan X, Zhang L, Zhang G, Zhu J (2015) Geodetic model of the 2015 April 25 M_w 7.8 Gorkha Nepal Earthquake and M_w 7.3 aftershock estimated from InSAR and GPS data. Geophys J Int 203:896–900. doi:10.1093/gji/ggv335

Galetzka J, Melgar D, Genrich JF, Geng J, Owen E, Lindsey EO, Xu X, Bock Y, Avouac JP, Adhikari LB, Upreti BN, Pratt-Sitaula B, Bhattarai TN, Sitaula BP, Moore A, Hudnut KW, Szeliga W, Normandeau J, Fend M, Flouzat M, Billinger L, Shrestha P, Koirala B, Gautam U, Bhatterai M, Gupta R, Kandel T, Timsina C, Sapkota SN, Rajaure S, Maharjan N (2015) Slip pulse and resonance of the Kathmandu basin during the 2015 Gorkha earthquake. Nepal. Science 349:1091–1095. doi:10.1126/science.aac6383

Government of Nepal (2015) Nepal Earthquake 2015: disaster relief and recovery information platform. http://apps.geoportal.icimod.org/ndrrip/

Grandin R, Vallée M, Satriano C, Lacassin R, Klinger Y, Simoes M, Bollinger L (2015) Rupture process of the $M_w = 7.9$ 2015 Gorkha earthquake (Nepal): insights into Himalayan megathrust segmentation. Geophys Res Lett 42. doi:10.1002/2015GL066044

Hayes GP, Briggs RW, Barnhart WD, Yeck WL, McNamara DE, Wald DJ, Nearly JL, Benz HM, Gold RD, Jaiswal KS, Marano K, Earle PS, Hearne MG, Smoczyk GM, Wald LA, Samsonov SV (2015) Rapid characterization of the 2015 M_w 7.8 Gorkha, Nepal, earthquake sequence and its seismotectonic context. Seismol Res Lett 86:1557–1567. doi:10.1785/0220150145

Hikima K, Koketsu K (2005) Rupture processes of the 2004 Chuetsu (mid-Niigata prefecture) earthquake, Japan: a series of events in a complex fault system. Geophys Res Lett 32:L18303. doi:10.1029/2005GL023588

Khattri KN (1987) Great earthquakes, seismicity gaps and potential for earthquake disaster along the Himalaya plate boundary. Tectonophysics 138:79–92. doi:10.1016/0040-1951(87)90067-9

Kikuchi M, Kanamori H (2003) Note on teleseismic body-wave inversion program. http://www.eri.u-tokyo.ac.jp/ETAL/KIKUCHI/

Kobayashi T, Morishita Y, Yarai H (2015) Detailed crustal deformation and fault rupture of the 2015 Gorkha earthquake, Nepal, revealed from ScanSAR-based interferograms of ALOS-2. Earth Planets Space 67:201. doi:10.1186/s40623-015-0359-z

Kohketsu K (1985) The extended reflectivity method for synthetic near-field seismograms. J Phys Earth 33:121–131. doi:10.4294/jpe1952.33.121

Kubo H, Dhakal YP, Suzuki W, Kunugi T, Aoi S, Fujiwara H (2016) Estimation of the source process of the 2015 Gorkha, Nepal, earthquake and simulation of long-period ground motions in the Kathmandu basin using a one-dimensional basin structure model. Earth Planets Space 68:16. doi:10.1186/s40623-016-0393-5

Lindsey EO, Natsuaki R, Xu X, Shimada M, Hashimoto M, Melgar D, Sandwell DT (2015) Line of sight deformation from ALOS-2 interferometry: M_w 7.8 Gorkha earthquake and M_w 7.3 aftershock. Geophys Res Lett 42:6655–6661. doi:10.1002/2015GL065385

Mugnier JL, Gajurel A, Huyghe P, Jayangondaperumal R, Jouanne F, Upreti B (2013) Structural interpretation of the great earthquakes of the last millennium in the central Himalaya. Earth Sci Rev 127:30–47. doi:10.1016/j.earscirev.2013.09.003

Murotani S, Miyake H, Koketsu K (2008) Scaling of characterized slip models for plate-boundary earthquakes. Earth Planets Space 60:987–991. doi:10.1186/BF03352855

Reasenberg PA, Simpson RW (1992) Response of regional seismicity to the static stress change produced by the Loma Prieta earthquake. Science 255:1687–1690. doi:10.1126/science.255.5052.1687

Sapkota SN, Bollinger L, Klinger Y, Tapponnier P, Gaudemer Y, Tiwari D (2013) Primary surface ruptures of the great Himalayan earthquakes in 1934 and 1255. Nat Geosci 6:71–76. doi:10.1038/ngeo1669

Szeliga W, Hough S, Martin S, Bilham R (2010) Intensity, magnitude, location, and attenuation in India for felt earthquakes since 1762. Bull Seismol Soc Am 100:570–584. doi:10.1785/0120080329

Takai N, Shigefuji M, Rajaure S, Bijukchhen S, Ichiyanagi M, Dhital MR, Sasatani T (2016) Strong ground motion in the Kathmandu Valley during the 2015 Gorkha, Nepal, Earthquake. Earth Planets Space 68:10. doi:10.1186/s40623-016-0383-7

Wang K, Fialko Y (2015) Slip model of the 2015 Mw 7.8 Gorkha (Nepal) earthquake from inversions of ALOS-2 and GPS data. Geophys Res Lett 42:7452–7458. doi:10.1002/2015GL065201

Wessel P, Smith WHF (1991) Free software helps map and display data. EOS Trans AGU 72:441

Yagi Y, Okuwaki R (2015) Integrated seismic source model of the 2015 Gorkha, Nepal, earthquake. Geophys Res Lett 42:6229–6235. doi:10.1002/2015GL064995

Yoshida S, Koketsu K, Shibazaki B, Sagiya T, Kato T, Yoshida Y (1996) Joint inversion of near- and far-field waveforms and geodetic data for the rupture process of the 1995 Kobe Earthquake. J Phys Earth 44:437–454. doi:10.4294/jpe1952.44.437

Zhu L, Rivera LA (2002) A note on the dynamic and static displacements from a point source in multilayered media. Geophys J Int 148:619–627. doi:10.1046/j.1365-246X.2002.01610.x